Forces in nematic liquid crystals constrained to the nanometer scale under hybrid anchoring conditions

B. Zappone,[1,2,*] Ph. Richetti,[2] R. Barberi,[1] R. Bartolino,[1] and H. T. Nguyen[2]
[1]*Liquid Crystals Laboratory (Cemif. Cal.–Università della Calabria), Ponte P. Bucci, cubo 33b, 87036 Arcavacata di Rende (CS), Italy*
[2]*Centre de Recherche Paul Pascal (CNRS–Université Bordeaux 1), Avenue Schweitzer, 33600 Pessac, France*
(Received 7 August 2004; published 11 April 2005)

Using a surface forces apparatus we have studied two thermotropic nematic liquid crystals (5CB and ME10.5) subjected to hybrid (homeotropic/planar) anchoring conditions. A film of nematic material is constrained between two curved smooth surfaces separated by less than 2500 Å. The intersurface force is nonmonotonic with the separation, being repulsive for thicknesses larger than $\simeq$100 Å and strongly adhesive at a shorter scale. While the repulsion can be qualitatively explained by an elastic model of director deformation, including anchoring deviation at the boundaries, the attraction cannot be explained either by elasticity or by dispersive forces. The expected confinement-induced anchoring transition has not been observed for a thickness as small as 200 Å.

DOI: 10.1103/PhysRevE.71.041703 PACS number(s): 61.30.Hn, 07.10.Pz

I. INTRODUCTION

Understanding the interfacial properties of nematic liquid crystals is a challenge for researchers working on soft matter and it is also relevant to control and improve the performances of the optical devices based on these materials. Most of the methods to characterize surface properties are based on the application of an electric or magnetic field, distorting the bulk nematic director towards a conformation incompatible with the equilibrium configuration imposed by the surfaces. This results in some *field-induced* textural transitions (i.e., the Fréedericksz transition [1]) occurring at a field intensity high enough to overcome the orientation imposed by the surfaces (the "anchoring"). The strength of the nematic/surface interaction is thus deduced by comparison. Following a similar approach, one can investigate the surface properties of a nematic from *confinement-induced* textural transitions, produced without applying any field. A classic example is the wedge-cell method used for measuring anchoring energies in twisted-planar or hybrid planar/homeotropic nematics [2]. The walls of the cell are treated to induce competing anchoring conditions, resulting in a distorted configuration. Moving along the wedge, one can study the thickness dependence of the director configuration. In particular, a confinement-induced *anchoring transition* is expected at a sufficiently short thickness, leading to a uniform director configuration aligned along the easy axis of the stronger anchoring [3]. The anchoring transition has been indeed observed in hybrid wedge cells [2] for weak anchoring energies ($W \simeq 10^{-5}$ J/m^2). Indirect evidence of this phenomenon has also been reported for other "field-off" techniques (thin-film balance [4], light scattering [5], ellipsometry [6,7]). The critical thickness for the transition depends on the anchoring strength and varies from a few μm for weak anchoring energies [2,5] to about 100 Å for stronger anchoring [6,7].

The surface force apparatus (SFA) allows the study of the confinement effects in liquid crystals in a more controlled way and at a much smaller length scale than other techniques. The SFA measurements on liquid crystals have focused so far on symmetrical homeotropic or planar cells, to study layering structuration [8–11] or friction properties [12,13] at a short scale ($\simeq$100 Å). The medium- and long-range responses have been studied for twisted nematics [8,10,11], but the results are still poorly understood. We report here SFA measurements on hybrid planar/homeotropic nematics, for which a strongly distorted configuration and an anchoring transition are expected. We will first introduce the SFA technique and describe a unique method to determine the director configuration across the confinement from multiple-beam interferometric data (Sec. II). Then, we will present a model for the elastic forces and the confinement-induced anchoring transition (Sec. III), to be compared to the experimental data of Sec. IV. The comparison (Sec. V) shows that the elastic theory fails in explaining the observed behavior at a length scale of a few hundred Å. An order reconstruction into a biaxial texture is proposed instead.

II. METHODS AND MATERIALS

A. Surface force apparatus

The optical characterization of the nematic samples and the force measurements were performed with a surface forces apparatus [14] (mark IV type [15]). A droplet of a nematic material is put by capillarity between two sheets of muscovite mica, glued onto cylindrical glass lenses of radius $R \simeq 2$ cm. The volume of the droplet is about 100 μl, the diameter of its circular section A in the middle plane between cylinders is about 1 cm, and the thickness at the droplet-air interface is $H \simeq 1$ mm. The muscovite mica has a stratified crystalline structure, that can be easily cleaved by hand to obtain large flexible sheets ($\simeq$1 cm^2) of uniform thickness (2–5 μm), exposing to the liquid crystal a clean and molecularly smooth surface (roughness 1 Å). The curved mica

*Electronic address: zappone@fis.unical.it

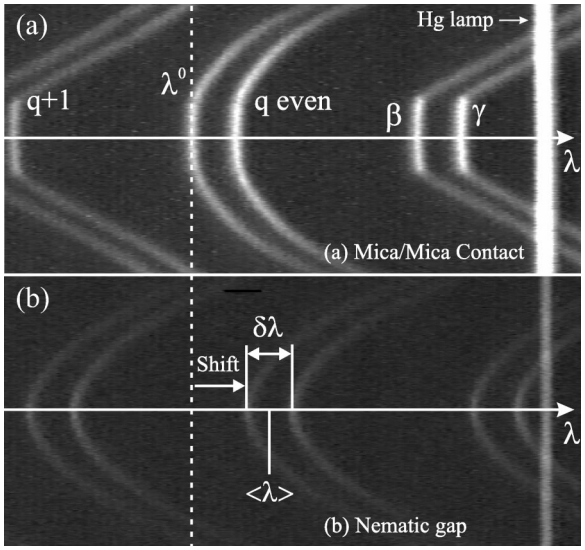

FIG. 1. Spectrograms showing a series of interference fringes of different chromatic order q. (a) Mica/mica contact in air ($D=0$). The contact region is flattened due to a strong adhesion. The fringes are split in doublets due to mica birefringence. (b) Nematic film of thickness $D>0$ between the mica surfaces. The average wavelength $\langle\lambda\rangle$ of the doublets is redshifted from the contact value λ^0. The doublet splitting $\delta\lambda$ depends on the birefringence of the mica and of the nematic and on the relative orientation of their optical axes.

sheets face each other in a crossed-cylinder geometry at a distance D apart. The surfaces are mounted in a stainless-steel sealed chamber and kept at a fixed temperature with a precision of about 0.05 °C. The upper surface can be moved vertically with an accuracy of a few Å by means of a piezoelectric tube translator. The lower surface is attached to a double cantilever spring of known stiffness ($k=10^2-10^3$ N/m), whose deflection is proportional to the force F acting between the surfaces. The force sensitivity is $10^{-7}-10^{-6}$ N. Separations D such that $dF/dD>k$ are mechanically unstable and give rise to "jumps" between stable regions [15].

B. Multiple-beam interferometry

The mica/mica separation D is measured by a multiple-beam interferometry technique [16]. The mica sheets are coated by a partially reflecting silver layer of thickness 500–520 Å, evaporated on the side to be glued on the cylinders. When illuminated perpendicularly by a white-light beam, the Ag/mica/liquid multilayer acts like a curved interferometer, selectively transmitting the waves satisfying a particular resonance condition. The transmitted light is passed through the slit of a grating spectrometer, where it forms curved interference fringes reproducing the curved geometry of the confinement with a lateral resolution of about 10 μm (Fig. 1). The spectrometer is calibrated on the lines of Hg and Kr lamps and the wavelength resolution is better than 1 Å.

Before introducing the liquid droplet between the mica surfaces, we measure the transmitted wavelengths λ^0 at mica/mica contact in air ($D=0$). The fringes appear as doublets (Fig. 1), since cleaved mica sheets are almost uniaxially birefringent under normal illumination [13,17]. Hence, the light waves polarized along the fast axis β see a shorter optical path and resonate at shorter wavelengths λ^0_β than the waves polarized along the slow axis γ, that resonate at λ^0_γ. The doublet splitting $\delta\lambda^0=\lambda^0_\gamma-\lambda^0_\beta$ can be used to determine the angle ψ between the γ axes of the two mica sheets, since $\delta\lambda^0(\psi)=\delta\lambda^0(0)\cos\psi$ [18].

After introducing the liquid droplet, the interference fringes are shifted towards larger wavelengths than at mica/mica contact (Fig. 2). For isotropic liquids, the average wavelength $\langle\lambda\rangle=(\lambda_\gamma+\lambda_\beta)/2$ increases monotonically as D is increased, while the doublet splitting $\delta\lambda$ remains almost constant within the spectrometer resolution as long as $D<4000$ Å [see Fig. 2(b) for $\theta=90°$]. For a birefringent liquid crystal, the average wavelength $\langle\lambda\rangle$ still increases as D is increased, but the doublet splitting $\delta\lambda$ is not constant. This effect cannot be correctly described by the usual equations for isotropic liquids [16,19], since they do not take into account any nematic birefringence. Moreover, they do not consider the director orientation with respect to the mica optical axes [Fig. 2(a)] and, for hybrid nematics, the director distortion across the confinement. The optical response of nematics is better analyzed in term of matrices, as proposed by Rabinowitz [20]. The light waves in the nematic and in the mica sheets are represented as $2d$ vectors $\mathbf{A}$, formed by the field components along the direction of ordinary and extraordinary polarization. The propagation in the nematic and the reflection at the nematic/mica and mica/silver interfaces are described by 2×2 matrices. The effect of a complete interferometric loop is represented by a matrix M: a wave $\mathbf{A}$ at a particular point inside the nematic produces a wave $M\mathbf{A}$ at the same point after a double reflection on the Ag-coated mica surfaces. The initial wave $\mathbf{A}$ interferes constructively with $M\mathbf{A}$ and with the higher-order reflections when these reproduce $\mathbf{A}$ to a 2π phase shift. The resonating waves are thus eigenvectors of the loop matrix, $M\mathbf{A}=\Omega\mathbf{A}$, corresponding to eigenvalues $\Omega>0$.

In Fig. 2, we have plotted the doublet splitting $\delta\lambda$ against the average wavelength $\langle\lambda\rangle$ for a uniform nematic slab between two mica sheets with crossed optical axes. We notice that $\delta\lambda$ strongly depends on both the zenithal (out-of-plane) and azimuthal (in-plane) angles of the director alignment: $\delta\lambda$ can be monotonically increasing with $\langle\lambda\rangle$ [i.e., with D, Figs. 2(b) and 2(c)] or have a minimum or a zero [Fig. 2(d)]. To identify the director configuration, we have compared the experimental splitting curve $\delta\lambda$ to the response of an equivalent uniform sample, simulated by the 2×2 matrix method. The mean director orientation across the film thickness is supposed to be close to the equivalent uniform alignment giving the best agreement with the experimental data. To measure the separation D, we use the analytic formulas derived for isotropic liquids [16], with a choice of the refractive index giving the same $D(\lambda)$ dependence obtained by matrix calculations. We estimate the final resolution for D to a few Å for $D<1000$ Å.

C. Liquid-crystal orientation

We have studied two different nematics: the 5CB (4'-*n*-pentyl-4-cyanobiphenyl, purchased from Merck) and the

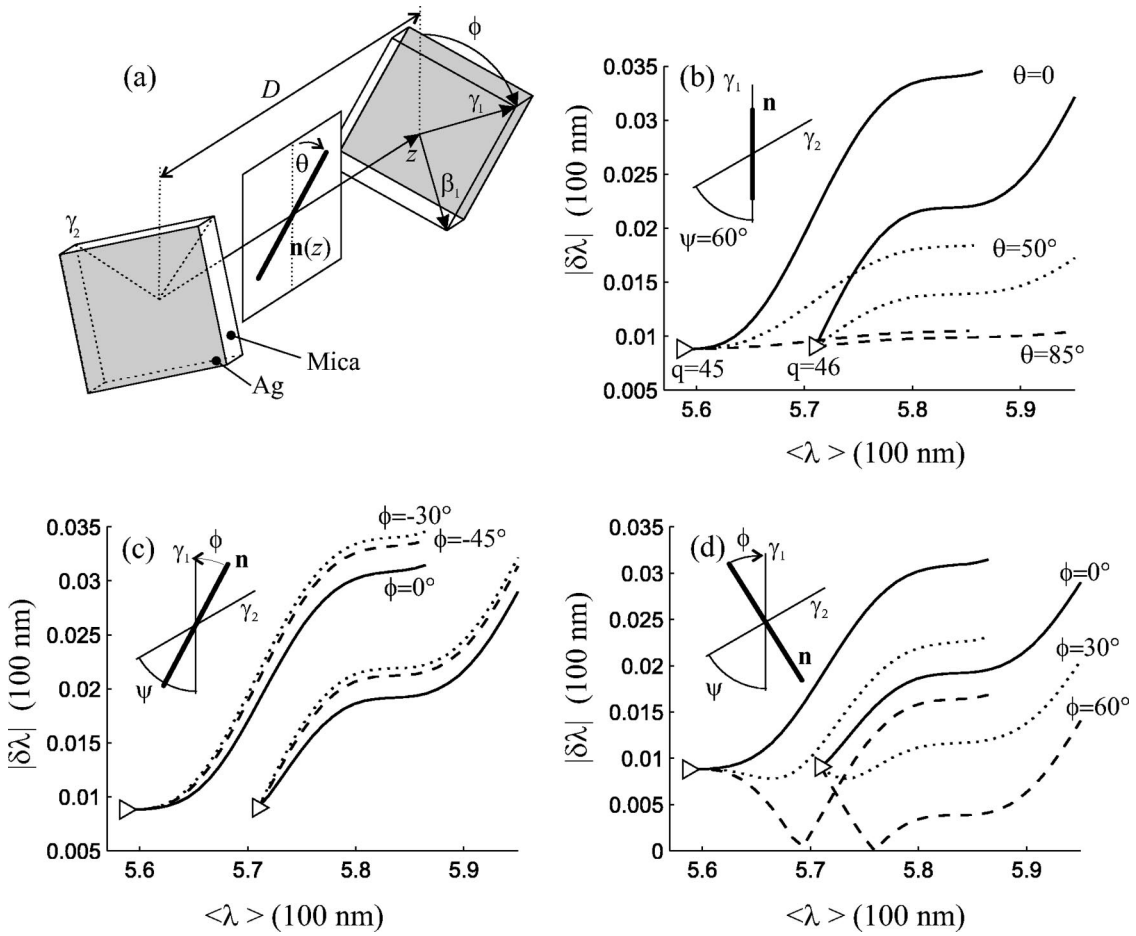

FIG. 2. (a) The mica sheets and the nematic director **n** around the contact point. (b) Doublet splitting $|\delta\lambda|$ vs average wavelength $\langle\lambda\rangle$ for a uniform sample in the range of separations 0–4000 Å. The azimuthal angle is fixed to $\phi=0$, while the zenithal angle θ is increased from a planar ($\theta=0$) to an almost homeotropic ($\theta=90°$) alignment. The latter configuration is nonbirefringent and equivalent to an isotropic liquid. The mica optical axes γ are crossed by $\psi=60°$. Two different chromatic orders $q=45$ and $q=46$ are shown. Triangles (▷) indicate values at mica/mica contact. (c) The zenithal angle is fixed to a uniform planar configuration, while the azimuthal orientation is varied. (d) Planar alignment along a direction outside the angle ψ. The nematic refractive indexes are $n_o=1.54$, $n_e=1.71$.

ME10.5/ZLI-0245 (4'-*n*-pentylphenyl-4-methoxybenzoate, synthesized in our laboratory). The anchoring of the 5CB on a freshly cleaved muscovite mica surface is planar, laying in a mirror plane σ at an angle $\alpha=\pm30°$ from the γ optical axis (Fig. 5, inset) [21–23]. The sign of α depends on the particular crystalline layer selected by the cleavage and cannot be determined *a priori*. To obtain the homeotropic anchoring, a monolayer of cationic surfactant CTAB (cetyl-trimethyl-ammonium-bromide) is adsorbed on the mica by dipping the surface for at least 30 min in a water solution at twice the critical micellar concentration [8,24]. The anchoring of ME10.5 on bare mica is also planar and the best homeotropic anchoring is obtained with the surfactant cetyl-tripropyl-ammonium-bromide, differing from CTAB only for the length of the lateral chains. In order to check the planar and homeotropic anchoring, preliminary observations have been done between crossed polarizers on two parallel thick mica plates, treated symmetrically to obtain a uniform planar or a homeotropic alignment. Then, interferometric measurements were performed on similar symmetrical SFA cells. The mica sheets are highly hydrophilic and get easily contaminated by ambient dust or volatile molecules. The micas were thus handled in a laminar flow cabinet at low humidity. To prevent adsorption-induced anchoring degradation and transitions [21–23], the surface was dried with a flux of N_2 for at least 1 h inside the sealed SFA chamber before putting the nematic droplet. A beaker containing about 1 g of desiccant P_2O_5 was kept inside the SFA chamber during the experiment, to keep the humidity as low as possible.

III. MODEL

A. Anchoring transition between flat parallel walls

Several years ago Barbero *et al.* [3] proposed a model to describe the confinement-induced anchoring transition, based on the Frank-Oseen elastic description of the nematic order. In a hybrid nematic slab constrained between two flat parallel walls inducing homeotropic and planar anchoring, the bulk splay/bend distortion can be reduced by a deviation of the surface director from the easy axes, due to finite anchoring energies of the Rapini-Papoular type [25]. The balance

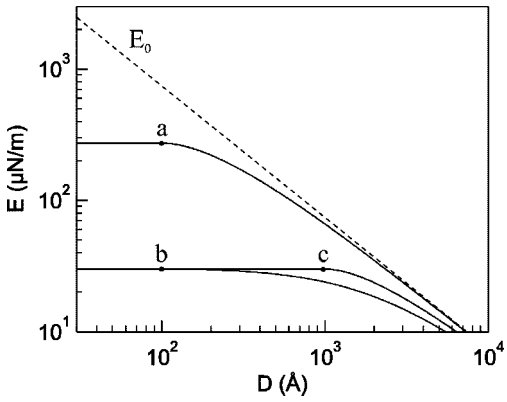

FIG. 3. Theoretical free energy E per unit area between flat parallel walls as a function of the separation D for different values of the extrapolation length (solid lines): (a) $L_h=110$ Å, $L_p=10$ Å; (b) $L_h=1000$ Å, $L_p=900$ Å; (c) $L_h=1000$ Å, $L_p=10$ Å. The dots mark the critical thickness for the anchoring transition, $D_c=|L_h-L_p|$, below which the energy is constant. The dashed line corresponds to the strong anchoring situation ($L_h=L_p=0$), where the energy E_0 scales as D^{-1}.

between the bulk elastic distortion (one-constant K approximation) and the surface deviation is determined by the extrapolation lengths $L_p=K/W_p$ and $L_h=K/W_h$, where W_p and W_h are the zenithal anchoring strengths for the planar and the homeotropic surface, respectively. For a separation D much larger than L_p and L_h the free energy per unit area is $E_0=(K/2)[(\pi/2)^2/D]$ as for infinitely strong anchoring (see Fig. 3). When in addition $D\gg\lambda$, the birefringence of the hybrid texture is about half the full value measured for a planar sample [2]. The surface deviation starts when the bulk elastic energy becomes comparable to the strength of the weaker anchoring. If we suppose the homeotropic anchoring to be weaker than the planar one, this occurs at $D'\simeq L_h$. When D reaches the critical value $D_c=|L_h-L_p|$, the sample undergoes a confinement-induced *anchoring transition* to a uniform alignment along the easy axis of the strongest anchoring [3]. For $D<D_c$, no additional force is required to vary the thickness of the uniform slab. Hence, the energy $E(D)$ reaches a plateau, corresponding to the energy required to align the weaker anchoring along the stronger easy axis (Fig. 3). Approaching the transition, the birefringence falls to zero for a uniform homeotropic alignment, or grows to the full value for a planar alignment.

B. Effects of curvature in the crossed-cylinder geometry

Figure 4 shows the anchoring geometry between two crossed cylinders of radius R inducing, respectively, a planar and a homeotropic anchoring, with infinite anchoring strengths. The ideal hybrid anchoring conditions, with a splay-bend director rotation of 90° across the thickness, is found only at the contact point. However, since the sense of rotation is not determined here, this point should correspond to a defect. In fact, a disclination line is expected to pass at the contact point, along a direction determined by the angle ξ between the planar easy axis σ and the cylinder axis [Figs. 4(a) and 4(b)]. We notice that a small tilt on one surface moves the disclination far from the contact point [Fig. 4(c)]. For example, a tilt as small as $\tau\simeq 3°$ produces a large displacement $x=R\sin\tau\simeq 1$ mm.

As we move far from the contact point, the hybrid anchoring conditions become more uniform if $\xi=0$ [Fig. 4(a)] or transform into twist if $\xi\neq 0$ [Figs. 4(b) and 4(d)], as a consequence of the surface curvature. In order to estimate the elastic force acting between the cylinders, we consider the simplest situation $\xi=0$. In the expression of the elastic free energy, we can neglect the horizontal derivatives along the axes x and y of the cylinders, since these are much more gradual than those along the vertical direction z. Calling $D+h$ and θ, respectively, the surface separation and the distortion angle at a point (x,y) [Fig. 4(c)], the splay-bend elastic energy in the one-constant approximation can be written as

$$E=\frac{K}{2}\int_A \frac{\theta(x,y)^2}{D+h(x,y)}dxdy. \tag{1}$$

The integral is extended to the circular area A of the nematic droplet in the xy plane, excluding the disclination line. In the presence of a tilt of a few degrees, the energy (1) changes only by a small amount, while the defect moves far from contact in a region where the surface separation is large. Hence the defect interacts weakly with the surfaces and the integral (1) is the only energy contribution relevant to the calculation of the elastic force. Since $\rho=A/\pi R^2\simeq 0.05$, in Eq. (1) we can expand θ and h in powers of x/R and y/R around the contact point $(x,y)=(0,0)$,

$$E=\frac{K}{2}\int_A \frac{(\pi/2-|x|/R)^2}{D+(x^2+y^2)/2R}dxdy. \tag{2}$$

Introducing the normalized variables ρ and $\delta=2D/R$, the integration gives

$$E=RK\left(\frac{\pi}{2}\right)^2\left[\left(\pi-\frac{2}{\pi}\delta\right)\log\left(1+\frac{\rho}{\delta}\right)+\frac{16}{\pi}\sqrt{\delta}\arctan\sqrt{\frac{\rho}{\delta}}+\frac{2}{\pi}\rho-\frac{16}{\pi}\sqrt{\rho}\right]. \tag{3}$$

Since in our SFA force measurements $\delta<10^{-5}$, Eq. (3) can be approximated as

$$E\simeq RK\left(\frac{\pi}{2}\right)^2\left[-\pi\log\delta+\frac{16}{\pi}\sqrt{\delta}+\pi\log\rho+\frac{2}{\pi}\rho-\frac{16}{\pi}\sqrt{\rho}\right]. \tag{4}$$

The vertical force between the surfaces is given by $F=-\partial E/\partial D-(\partial E/\partial A)(\partial A/\partial D)$. Assuming the volume of the droplet to be constant with D and the air-nematic interface to be cylindrical, in the approximation $\rho\ll 1$ we have [26]: $\rho\simeq\rho_0-\delta\simeq\rho_0$. Hence, the variation of ρ with δ is negligible compared to the contact value ρ_0 and $\partial\rho/\partial D$ does not depend on D. The force is thus simply given by

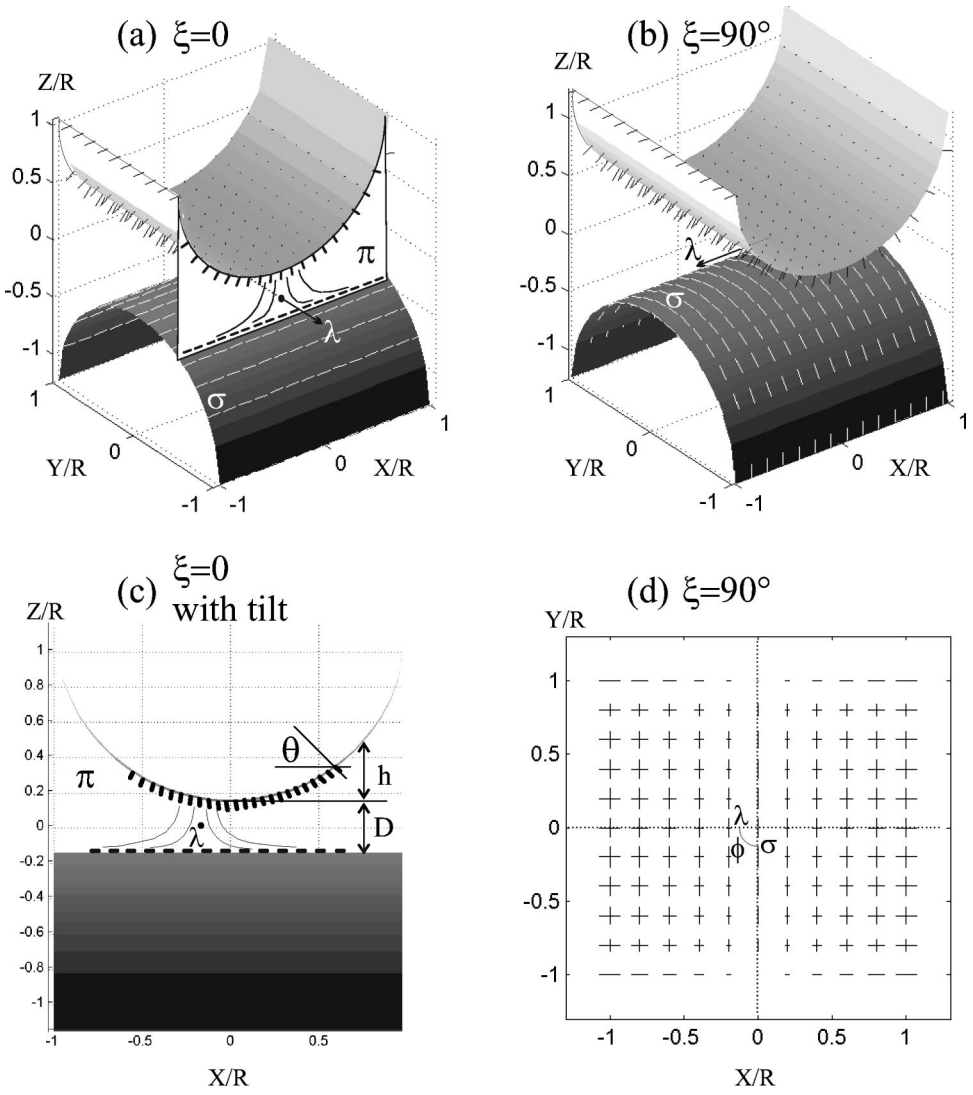

FIG. 4. Anchoring geometry and disclination line. (a,b) The direction of the disclination λ at the contact point depends on the angle ξ between the planar easy axis σ and the lower cylinder axis x. When $\xi=0$ the director configuration on the plane π is purely splay bend, otherwise a twist distortion must be considered. (c) Effect of a tilt of a few degrees on the homeotropic anchoring: λ do not pass at the contact point. (d) Top view of (b), showing the curvature-induced twist between the planar easy axis σ of the lower cylinder (in-plane component along y) and the homeotropic easy axis of the upper cylinder (component along x).

$$F \simeq 2\pi\left(\frac{\pi}{2}\right)^2\frac{K}{\delta} - 4\pi\frac{K}{\sqrt{\delta}}, \tag{5}$$

where we have neglected the terms depending only on ρ, which are negligible or vary too slowly with δ. The force (5) can be compared to other calculations, performed for twisted planar [8] and symmetrical homeotropic [26] anchoring conditions. In the former work [8], the anchoring conditions are supposed to be uniform throughout the sample. This corresponds to putting $\theta=\pi/2$ in Eq. (1) and leads to the first term in Eq. (5). This term is thus the effect of the *anchoring-induced* director deformation in the contact region. In the later work [26], on the contrary, the contact region is uniform and the force is due to a *curvature-induced* director deformation in the peripheral regions. This force depends on $K/\sqrt{\delta}$, as the second term of Eq. (5). Starting from the same symmetry considerations used in Ref. [26], it can be shown that the same result can be obtained directly from Eq. (2), imposing homeotropic anchoring conditions.

Since in a typical SFA experiment $\sqrt{\delta} \ll 1$, the curvature-induced terms in Eq. (5) can be neglected with respect to the anchoring-induced terms. In particular, the curvature-induced twist distortion, expected when $\xi \neq 0$, would contribute a negligible term to the total elastic energy. Hence, both the net elastic force F between crossed cylinders and the surface energy E_0 between parallel walls scale with $1/D$ when the anchoring is infinitely strong. In fact, F and E_0 are related by the Derjaguin relation $F/R=2\pi E_0$. The Derjaguin relation holds also for finite anchoring strengths as long as D is much larger than both extrapolation lengths (see Fig. 3). We stress that the Derjaguin relation is not valid for symmetrical homeotropic anchoring conditions [26], since it would lead to a zero force.

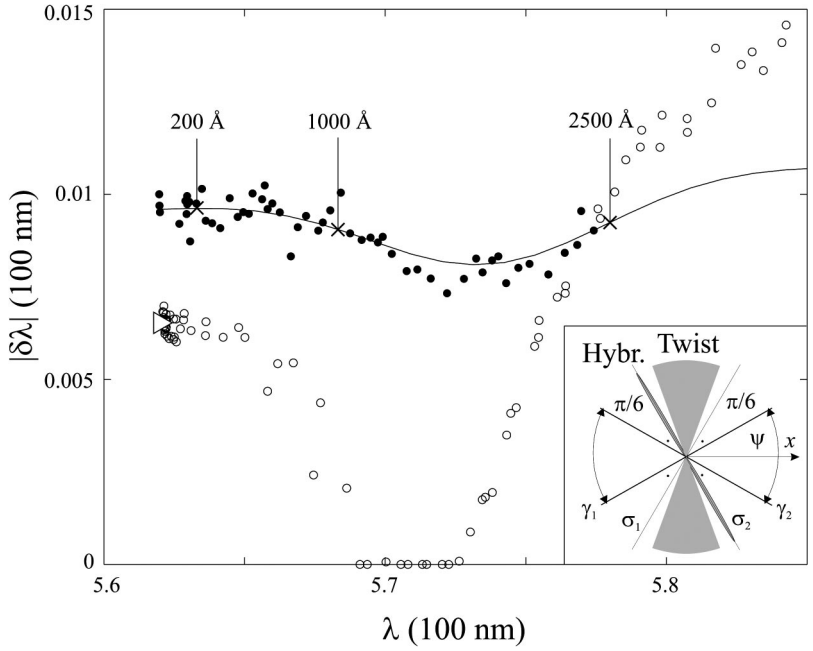

FIG. 5. Doublet splitting $|\delta\lambda|$ vs the average wavelength $\langle\lambda\rangle$ for a 5CB in twisted-planar ($\circ$) and hybrid ($\bullet$) anchoring conditions (temperature: 27.20 °C). The angle $\psi=56\pm5°$ between the γ optical axes is determined at mica/mica contact in air ($\triangleright$). The splitting at CTAB/mica contact is higher than for mica/mica contact, because the angle ψ was reduced of $\delta\psi\simeq12°$ when replacing the upper mica. Inset: schematic representation of the director configuration as viewed along the surface normal at the contact point. The γ_1 and γ_2 axes belong, respectively, to the upper (CTAB-treated) and lower (bare) mica. The gray areas represent the director distribution across the confinement. Solid line: simulation for a uniform tilted director laying in the plane σ_2 of the untreated mica. A cross on the solid line indicates a particular surface separation.

When the anchoring strengths are finite and D is comparable to one of the extrapolation lengths, the repulsion is weaker than for infinite strengths, since the elastic energy per unit area between parallel walls is weaker and less rapidly changing with D (see Fig. 3). Decreasing D below the critical thickness D_c of the anchoring transition, an increasing portion of the sample around the contact point becomes uniform and no longer contributes to the force. This situation is similar to the case of symmetrical homeotropic samples mentioned above [26]. The repulsion comes from the outer regions, where the director is still distorted under competing anchoring conditions. However, the anchoring is modified by the curvature and differs from the homeotropic/planar anchoring conditions in the central region. The net interaction is thus not expected to scale as the energy per unit area of the central region. Hence, we will not use the Derjaguin approximation when finite anchoring strengths or anchoring transition could be present, i.e., for separations comparable to the extrapolation lengths.

The finite value of the anchoring strengths also influence the defect line at the contact point. As long as there is a distortion in the central region, we expected a defect line similar to that described for infinite strengths. After the anchoring transition, the central region becomes uniform and no defect line is present.

IV. EXPERIMENTAL RESULTS

A series of experiments has been performed on different 5CB and ME10.5 samples, showing similar features in the force profiles and the optical response. Before putting the nematic droplet between the surfaces, the reference values of the transmitted wavelengths λ^0 at mica/mica contact and the angle ψ between the γ optical axes were determined by FECO interferometry. Then, one of the surfaces was removed from the SFA and dipped in the surfactant solution to obtain a homeotropic anchoring. When this surface was assembled again in the SFA, we usually changed the contact point and introduced an error $\delta\psi$ of a few degrees, that can be estimated from FECO data at surfactant/mica contact. Since the sign of the angle $\alpha=\pm30°$ between the planar easy axis σ and the γ axis of the untreated (planar) mica is *a priori* unknown, then the angle ξ between σ and the cylinder axis is also undetermined. The sign of α can be determined *a posteriori* from the FECO data in the presence of the nematic, while the value of ξ remains undetermined.

A. 5CB: Doublet splitting

In Fig. 5, the same drop of 5CB was studied under symmetrical planar and hybrid planar/homeotropic anchoring conditions. In the planar case, the easy axes σ are such that the mean director orientation minimizing the twist elastic energy is along the external bisector of ψ (Fig. 5, inset). This gives the doublet degeneracy (zero splitting) observed in Fig. 5, to be compared to the plots of Fig. 2(d). Under hybrid anchoring conditions, the splitting variation with D is slower than in the planar case and the zero is replaced by a minimum (Fig. 5). The sample is optically equivalent to a uni-

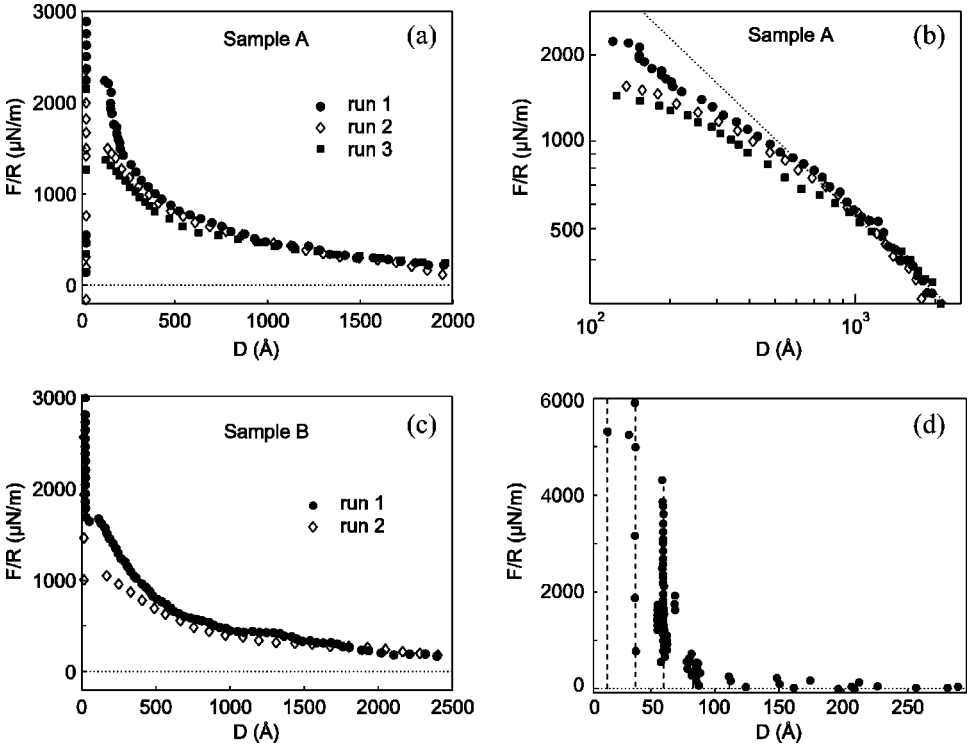

FIG. 6. Typical force profiles in hybrid 5CB samples. (a) The repulsion decreases with time as the surfaces are brought into contact repeatedly at the same contact point. The runs are numbered in chronological order. (b) The repulsion can be fitted with Eq. (5) and $K=6\times10^{-12}$ N for $D>700$ Å (dotted line). For smaller separation the force increase more slowly as D is decreased. (c) The repulsion degrades with time even if the contact point is changed (contact point a, b, etc.). (d) Example of layering oscillations in the final homeotropic configuration. The period is $\simeq$25 Å, corresponding to 5CB molecules normal to the layers [8,10]. Only the descending part of the oscillations is shown.

form tilted sample, with the director laying in the mirror plane σ of the untreated mica, at 30° from the γ optical axis.

The birefringence δn^* of the equivalent sample is about half the full value $\delta n=0.175$ for 5CB at the temperature and wavelengths λ considered [27]. This shows that a hybrid type of alignment is indeed obtained under competing homeotropic and/or planar anchoring conditions. However, the birefringence does not seem to fall to zero or grow to the full value down to separations as small as 200 Å. Hence, there is no anchoring transition for a separation $D>200$ Å. For a smaller thickness, the determination of the director orientation by FECO interferometry becomes unreliable.

We systematically observe a disclination line that runs aside the contact point at a distance of several tenths of μm.

B. 5CB: Force profiles

Figure 6 shows the typical nonmonotonic force profile of hybrid 5CB samples. As the separation is decreased down to 100–150 Å, the force is repulsive and smoothly increasing. The repulsion does not follow a simple power law: it can be fitted by Eq. (5) with the usual value [28] of $K=6\times10^{-12}$ N only for $D>700$ Å, while it increases more slowly at shorter separations [Fig. 6(b)]. For $D<100$–150 Å, the force rapidly decreases towards negative value as separation is decreased. This leads to a jump to contact and to a strong adhesion at very short separations (20–30 Å). Due to the limited extension of the piezoelectric tube, it was not possible to pull the two surfaces apart from the contact and measure the adhesion. At very short separations, we do not observe any layering structuration of the type described in Refs. [8,10,11] for symmetrical planar or homeotropic anchoring conditions.

The hybrid 5CB samples are subjected to a degradation with time. The alignment tends to become uniform homeotropic, showing zero birefringence and a SmA-type layering structuration [Fig. 6(d)] [8,10] at very short range. The evolution appears in the force profiles as a progressive diminution of the repulsion intensity, while the position and length of the jump to contact do not vary with time. On the contrary, symmetrical planar samples do not show any changes in the anchoring conditions. We ascribe the behavior of the hybrid samples to a progressive contamination of the untreated mica by the cationic surfactant, desorbed from CTAB-coated mica into the highly polar 5CB. The transfer is probably enhanced by the repeated contacts between the treated and untreated surfaces.

C. ME10.5

The splitting curves and force profiles obtained for hybrid ME10.5 samples are similar to those obtained for hybrid 5CB. The optical response is equivalent to that of a tilted uniform director laying in the σ plane of the untreated mica

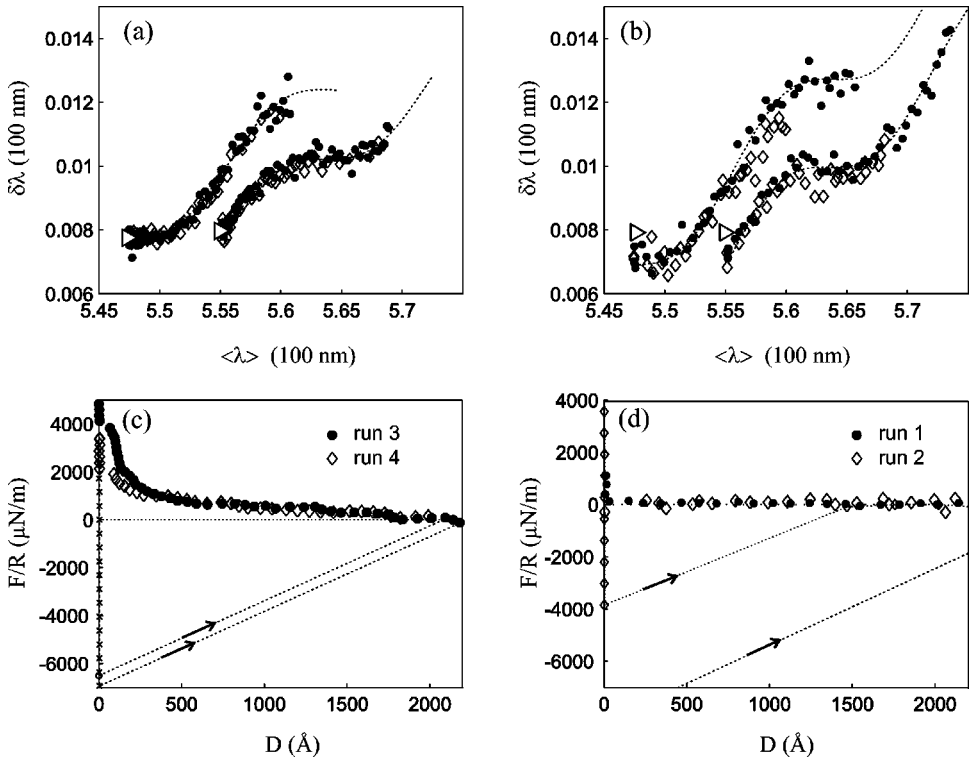

FIG. 7. (a,b) Doublet splitting $|\delta\lambda|$ vs the average wavelength $\langle\lambda\rangle$ for a hybrid ME10.5 sample at different contact points. The angle $\psi=63\pm5°$ is determined at mica/mica contact in air (▷). The dotted line is the optical response of a uniform tilted sample, with the director laying in the mirror plane σ of the untreated mica surface. (b,c) Force profiles corresponding to (a) and (b). The force runs are numbered in chronological order. Notice that the repulsion increases when the contact point is changed. The arrows mark the jumps out from contact.

[Figs. 7(a) and 7(b)]. The birefringence $\delta n^*=0.06$ is close to but slightly smaller than half the full value $\delta n=0.13$ [29], suggesting a hybrid alignment. We do not observe any defect line passing at the contact point, as for the hybrid 5CB.

The force profiles [Fig. 7(c)] qualitatively show the same features as the 5CB: a long-range repulsion increasing more slowly as D is decreased and a short-range attraction, leading to a jump to contact at $D\simeq100$ Å and to a strong adhesion at contact, without any layering structuration at very short range. The measurements shown in Fig. 7 have been performed with a stiffer cantilever and a wider piezoelectric tube extension than for 5CB samples, allowing the two surfaces to be pulled apart from adhesion. The adhesive force varied in the range from -8 to -2 mN/m.

Since the ME10.5 is less polar than 5CB, the surfactant desorption is expected to be weaker and slower. In fact, we never observe a global evolution towards homeotropic anchoring conditions as for 5CB hybrid samples. Nevertheless, we still observe a diminution of the repulsion in time, as we repeatedly bring the surfactant-coated and the bare mica surfaces into contact at the same point. Moreover, the intensity of the repulsion changes when the contact point is changed, suggesting a nonhomogeneous surface treatment, while the doublet splitting curve and the short-range attraction do not vary significantly.

V. DISCUSSION

The hybrid samples studied in our experiments showed systematically a disclination line, passing several tenths of μm away from the contact point. The defect does not seem to affect the director configuration near the contact point that is determined by the local anchoring conditions. It is likely that the disclination is removed from the contact point by a small tilt on the homeotropic surface, where the surfactant monolayer could be insufficient to completely screen the planar anchoring induced by the underlying mica [30].

While the interferometric data ensure that an intermediate type of alignment is effectively created in 5CB and ME10.5 under hybrid anchoring conditions, there is no direct evidence of a confinement-induced anchoring transition in these samples for separations as small as 200 Å. Hence, according to the model by Barbero *et al.* [3], an upper bound for the critical thickness should be fixed at $D_c=|L_p-L_h|<200$ Å. Can we deduce the absolute value of the extrapolation lengths from FECO optical data only? When L_p and L_h are much shorter than D, then a splay-bend distortion is the preferred configuration, where a strong anchoring opposes the strong elastic torque imposed by the bulk. On the contrary, when $L_p, L_h \gg D$, the sample is almost uniformly tilted, with both anchoring directions strongly deviated from their easy axes. The director average orientation across the confinement is similar in the two cases and the optical behavior should also be comparable. Hence, we cannot determine the anchoring strengths from FECO interferometry only and we must look at the repulsive part of the force profiles.

The observed repulsion extends up to several hundreds of Å and scales as $1/D$ at large separations. Since we have a droplet, with changing nematic/air and nematic/mica interfacial areas as D is changed, we must consider capillary forces

and surface tension. However, D is much smaller compared to any other length specifying the geometry of the droplet. Hence, the interfacial areas are almost constant with D, rather than scaling as $1/D$. As an example, consider a droplet between two spheres of radius R separated by a distance D. Suppose the air/droplet interface to be a cylinder of height $H_0 \simeq 1$ mm for $D=0$. As D is increased to a few hundred nm, the height is almost constant, scaling as $H \simeq H_0 + D/2 \simeq H_0$, as well as the area S_c of the spherical caps wet by the droplet and the air/droplet lateral surface S_l, scaling, respectively, as $S_c \simeq \pi RH$ and $S_l/4\pi R^2 \simeq \sqrt{(H/R)^3/4 - (H/R)^4/16}$.

The observed repulsion is to be attributed to an elastic director distortion induced by the competing homeotropic and planar anchoring. Moreover, the $1/D$ dependence at large separation suggests that fixed boundary conditions must be considered in this range. As the separation is further decreased down to about 700 Å, the repulsion increases more slowly with D, suggesting a finite value of the anchoring energies (see Fig. 3). The planar anchoring strength on muscovite mica is known to be particularly strong [30] ($W_p \simeq 0.1$ mJ/m^2), while reported values for the homeotropic anchoring are usually weaker [31,32] ($W_h \lesssim 0.01$ mJ/m^2). Hence, the weakening of the repulsion could be the effect of a homeotropic extrapolation length L_h of about 700 Å or less. Since the critical thickness is bound to $D_c = L_h - L_p < 200$ Å, the planar extrapolation length is given by: $L_h \geqslant L_p \geqslant L_h - 200$ Å. The value of the homeotropic anchoring ($W_h \gtrsim 0.1$ mJ/m^2) turns out to be higher than the typical values reported in the literature [31,32]. There are no other measurements of W_h for a biphenyl nematic on a crystalline mica surface covered by a monolayer of surfactant. The energy strengths are usually measured on glass substrates, covered by specific aligning layers, applying to the nematic sample an external electric or magnetic field. We can compare our results to "field-off" ellipsometry experiments, performed on microscopic nematic droplets spreading on a silicon substrate under hybrid homeotropic and/or planar anchoring conditions [6,7]. The spreading reduces the droplet thickness down to a critical value, where a structural transition is observed, similar to the anchoring transition. Far from the nematic-isotropic transition, the measured critical thickness is about 100 Å and both planar and homeotropic anchoring strengths are found to be higher than 0.1 mJ/m^2, as in our case.

The most surprising result in our experiment is the presence of a strong attraction at separations $D < 100$ Å, probably related to the high strength of the anchoring. In fact, the attraction is not elastic, since director deformations always produce repulsion. We have also calculated the van der Waals force for a nematic and/or surfactant slab between flat parallel mica surfaces [33], choosing the mean value for the refractive index and the dielectric constant of the anisotropic liquid crystal. The force turns out to be attractive, but its range is too short (a few nm) and its intensity too weak to explain the observed attraction at $D \simeq 100$ Å. Following the results of recent works on the stability of thin hybrid nematic films on silicon substrates [34,35], we have also considered possible structural forces deriving from order gradients and fluctuations (pseudo-Casimir forces) across the confinement. These forces, however, are relevant only when the hybrid sample has already undergone the anchoring transition to a uniform configuration. When the sample is still hybrid at a separation of the order of 100 Å, as in our case, the gradient and fluctuation forces cannot compete with the elastic force.

The attraction observed in our experiment could be explained as a confinement-induced structural transition from the usual splay-bend uniaxial configuration into a biaxial texture, known as "director-exchange" configuration [36–40]. In this configuration, a thin biaxial layer divides the sample in two, almost uniform, uniaxial regions, aligned along the easy axis of the nearest wall. The transition into the biaxial texture has been predicted between two flat parallel walls, when the imposed stress and both anchoring strengths are high, as in our case. Recently, the dynamics of order reconstruction associated with a biaxial transition has been studied theoretically and experimentally for thin nematic cells of fixed thickness subjected to a strong electric field [41,42]. Biaxial textures cannot be described by the Frank-Oseen elastic theory. Only a complete tensor-order Landau–De Gennes model can correctly describe the nematic order at a scale comparable to the nematic correlation length, typically 10-nm away from the nematic-isotropic phase transition [1]. Such a tensor-order approach for the curved confinement geometry of the SFA is beyond the aim of this paper. Nevertheless, we notice that the director-exchange structure in hybrid samples should have a birefringence similar to the usual splay-bend configuration. Hence, a confinement-induced order reconstruction between the two structures could have negligible effects on the interferometric response, explaining the constant birefringence observed in our experiments. Moreover, recent force calculations carried out in the framework of the Landau–De Gennes theory [43] show that the order reconstruction should be associated with a nonmonotonic or discontinuous force profile, as observed in our experiments.

VI. CONCLUSIONS

Force measurement in liquid crystals is a way of measuring the confinement properties of these materials at the nanometer scale without applying external fields. These first SFA measurements on hybrid nematic films show that the elastic description of the nematic order is not sufficient to explain the observed behavior at a length scale smaller than a few hundred Å. At long range ($D > 100$ Å), the force is determined by the elastic response of the nematic material and by the value of the anchoring energies. At short range ($D < 100$ Å) we observe unexpected features, probably related to an order reconstruction into a biaxial texture. More theoretical and experimental work is needed to clarify this point. In particular, experiments are in progress to improve the stability of the homeotropic anchoring on muscovite mica using chemisorbed surfactants.

[1] P. G. D. Gennes, *The Physics of Liquid Crystals* (Clarendon, Oxford, 1975).
[2] G. Barbero, N. V. Madhusudana, and G. Durand, J. Phys. (France) Lett. **45**, L613 (1984).
[3] G. Barbero and R. Barberi, J. Phys. (Paris) **44**, 609 (1983).
[4] J. E. Proust and L. Ter-Minassian-Saraga, J. Phys. (Paris), Colloq. **4**, 490 (1979).
[5] M. M. Wittebrood, T. Rasing, S. Stallinga, and I. Musevic, Phys. Rev. Lett. **80**, 1232 (1998).
[6] M. P. Valignat, S. Villette, J. Li, R. Barberi, R. Bartolino, E. Dubois-Violette, and A. M. Cazabat, Phys. Rev. Lett. **77**, (1996).
[7] F. Vandenbrouck, M. P. Valignat, and A. M. Cazabat, Phys. Rev. Lett. **82**, 2693 (1999).
[8] R. G. Horn, J. N. Israelachvili, and E. Perez, J. Phys. (Paris) **42**, 39 (1981).
[9] P. Richetti, L. Moreau, P. Barois, and P. Kekicheff, Phys. Rev. E **54**, 1749 (1996).
[10] M. Ruths, S. Steinberg, and J. Israelachvili, Langmuir **12**, 6637 (1996).
[11] M. Ruths and S. Granick, Langmuir **16**, 8368 (2000).
[12] J. Janik, R. Tadmor, and J. Klein, Langmuir **17**, 5476 (2001).
[13] A. Artsyukhovich, L. D. Broekman, and M. Salmeron, Langmuir **15**, 2217 (1999).
[14] J. N. Israelachvili and D. Tabor, Proc. R. Soc. London **A331**, 19 (1972).
[15] J. L. Parker, H. K. Christenson, and B. W. Ninham, Rev. Sci. Instrum. **60**, 3135 (1989).
[16] J. N. Israelachvili, J. Colloid Interface Sci. **44**, 259 (1973).
[17] V. Kitaev and E. Kumacheva, J. Phys. Chem. B **104**, 8822 (2000).
[18] P. M. McGuiggan and J. N. Israelachvili, J. Mater. Res. **5**, 2232 (1990).
[19] R. G. Horn and D. T. Smith, Appl. Opt. **30**, 59 (1991).
[20] P. Rabinowitz, J. Opt. Soc. Am. A **12**, 1593 (1995).
[21] P. Pieranski and B. Jerôme, Phys. Rev. A **40**, 317 (1989).
[22] J. Bechofer, J. L. Duvail, L. Masson, B. Jerôme, R. M. Hornreich, and P. Pieranski, Phys. Rev. Lett. **64**, 1911 (1990).
[23] B. Jerôme, Rep. Prog. Phys. **54**, 391 (1991).
[24] Y. L. Chen, S. Chen, C. Frank, and J. Israelachvili, J. Colloid Interface Sci. **153**, 244 (1992).
[25] A. Rapini and M. Papoular, J. Phys. (Paris), Colloq. **30**, 54 (1969).
[26] A. M. Sonnet and T. Gruhn, J. Phys.: Condens. Matter **11**, 8005 (1999).
[27] I. C. Koo and S. T. Wu, *Optics and Nonlinear Optics of Liquid Crystals* (World Scientific, Singapore, 1993).
[28] N. V. Madhusudana and R. Pratibha, Mol. Cryst. Liq. Cryst. **89**, 249 (1982).
[29] I. H. Ibrahim and W. Haase, J. Phys. (Paris) **40**, 191 (1979).
[30] L. M. Blinov and A. A. Sonin, Mol. Cryst. Liq. Cryst. **179**, 13 (1990).
[31] L. M. Blinov and V. Chigrinov, *Electrooptic Effects in Liquid Crystals* (Springer, Berlin, 1994).
[32] B. Jerôme, Rep. Prog. Phys. **54**, 391 (1991).
[33] J. Israelachvili, *Intermolecular and Surface Forces* (Academic, New York, 1985).
[34] A. Sarlah, P. Ziherl, and S. Zumer, Mol. Cryst. Liq. Cryst. Sci. Technol., Sect. B: Nonlinear Opt. **36**, 443 (2001).
[35] P. Ziherl, R. Podgornik, and S. Zumer, Phys. Rev. Lett. **84**, 1228 (2000).
[36] P. Palffy-Muhoray, E. C. Gartland, and J. Kelly, Liq. Cryst. **16**, 713 (1994).
[37] H. G. Galabova, N. Kothekar, and D. W. Allender, Liq. Cryst. **23**, 803 (1997).
[38] A. Sarlah and S. Zumer, Phys. Rev. E **60**, 1821 (1999).
[39] I. Rodriguez-Ponce, J. M. Romero-Enrique, and L. F. Rull, Phys. Rev. E **64**, 051704 (2001).
[40] F. Bisi, E. C. Gartland, R. Rosso, and E. G. Virga, Phys. Rev. E **68**, 021707 (2003).
[41] R. Barberi, F. Ciuchi, G. E. Durand, M. Iovane, D. Sikharulidze, A. M. Sonnet, and E. G. Virga, Eur. Phys. J. E **13**, 61 (2004).
[42] R. Barberi, F. Ciuchi, G. Lombardo, R. Bartolino, and G. E. Durand, Phys. Rev. Lett. **93**, 137801 (2004).
[43] F. Bisi, E. Virga, and G. Durand, Phys. Rev. E **70**, 042701 (2004).